

Modeling Coupled Evaporation and Seepage in Ventilated Cavities

T. A. Ghezzehei,* R. C. Trautz, S. Finsterle, P. J. Cook, and C. F. Ahlers

ABSTRACT

Cavities excavated in unsaturated geological formations are important to activities such as nuclear waste disposal and mining. Such cavities provide a unique setting for simultaneous occurrence of seepage and evaporation. Previously, inverse numerical modeling of field liquid-release tests and associated seepage into cavities were used to provide seepage-related large-scale formation properties, ignoring the impact of evaporation. The applicability of such models was limited to the narrow range of ventilation conditions under which the models were calibrated. The objective of this study was to alleviate this limitation by incorporating evaporation into the seepage models. We modeled evaporation as an isothermal vapor diffusion process. The semi-physical model accounts for the relative humidity (RH), temperature, and ventilation conditions of the cavities. The evaporation boundary layer thickness (BLT) over which diffusion occurs was estimated by calibration against free-water evaporation data collected inside the experimental cavities. The estimated values of BLT were 5 to 7 mm for the open underground drifts and 20 mm for niches closed off by bulkheads. Compared with previous models that neglected the effect of evaporation, this new approach showed significant improvement in capturing seepage fluctuations into open cavities of low RH. At high relative-humidity values (>85%), the effect of evaporation on seepage was very small.

SEEPAGE OF LIQUID WATER into cavities is an important phenomenon for subsurface activities such as mining and geologic disposal of nuclear wastes. A key factor affecting the long-term safety of the proposed nuclear waste repository at Yucca Mountain (YM), Nevada, is the seepage of liquid water into waste emplacement cavities. The rate, chemical composition, and spatial and temporal distributions of seepage are critical factors that determine corrosion of waste canisters, integrity of engineered barriers, and dissolution and mobilization of contaminants and their release to groundwater (Bodvarsson et al., 1999; Finsterle et al., 2003). In unsaturated formations, capillary forces hold the pore water tightly in the formation and divert the flow around the cavity, thereby preventing seepage into the cavity. The barrier created by the capillary force is commonly known as a "capillary barrier." Philip and coworkers (Knight et al., 1989; Philip, 1989a, 1989b; Philip et al., 1989a, 1989b) considered steady-state unsaturated flow around capillary barriers and provided analytical solutions for the critical

conditions that trigger seepage into various idealized cavity geometries excavated in homogeneous formations. Detailed numerical models have been used to study unsaturated flow in heterogeneous fractured media and seepage into cavities of various geometries under transient conditions (e.g., Birkholzer et al., 1999; Finsterle, 2000; Finsterle and Trautz, 2001; Li and Tsang, 2003). Site-specific seepage models for the proposed nuclear waste repository at YM were developed by calibrating the effective seepage-related parameters against field seepage test data (Finsterle et al., 2003).

Most of the previous numerical models assumed that liquid water leaking into a cavity drips (seeps) immediately from the place of entry. The potential for evaporation to compete with seepage has been generally ignored, and its effect was lumped with the effective flow parameters of the unsaturated medium (Finsterle et al., 2003). In calibration of the analytical model of Philip et al. (1989b) against field seepage data, Trautz and Wang (2002) accounted for the effect of evaporation by adjusting the field seepage data for evaporation. Because the data were obtained from tests conducted in relatively humid cavities, the effect of evaporation on the calibrated seepage-related parameter was not significant. However, recent field measurements of seepage and free-water evaporation in ventilated cavities at YM have shown that seepage rate is significantly influenced by evaporation. The foregoing discussions suggest that the applicability of models that ignore evaporation is limited to similar humidity and temperature conditions under which the calibrations are performed (Finsterle et al., 2003). Such models cannot satisfactorily capture the seepage rate fluctuations when the seepage experiments are conducted under variable humidity and ventilation conditions. More importantly, seepage models that ignore evaporation and that are calibrated against seepage data under ventilated and/or low humidity conditions are not expected to perform well in predicting future (expected nonventilated and humid) seepage conditions. The preceding observations call for a calibrated seepage model that reliably performs over a wide range of ventilation and humidity conditions.

The objective of this study was to improve the portability of calibrated seepage models by reducing the impact of evaporation on the calibrated effective parameters. Thus, we propose to incorporate evaporation from cavity walls into the existing seepage models by assuming a first-order diffusion approximation.

EVAPORATION IN CAVITIES

Fundamentally, evaporation is a two-step process. The first step involves transition from liquid to vapor

T.A. Ghezzehei, R.C. Trautz, S. Finsterle, P.J. Cook, and C.F. Ahlers, Earth Sciences Division, Lawrence Berkeley National Laboratory, University of California, MS 90R1116, 1 Cyclotron Rd., Berkeley, CA 94720-8126; C.F. Ahlers, currently, LFR Levine Fricke, Costa Mesa, CA. Received 29 Sept. 2003. Special Section: Research Advances in Vadose Zone Hydrology through Simulations with the TOUGH Codes. *Corresponding author (TAGhezzehei@lbl.gov).

phase at the liquid–vapor interface (vaporization). The second step is the transport of vapor from the high concentration area at the evaporating surface to the low concentration area of the ambient air. Accurate modeling of these coupled processes is difficult for several reasons: (i) the first step is an endothermic phenomenon, and the parameters that govern this process are strongly temperature dependent; (ii) the vapor concentration gradient in the boundary layer is strongly influenced by the air flow regime; and (iii) the air flow depends on, among other things, the ambient wind velocity, local turbulence, and the roughness of the evaporating surface.

Ho (1997) and Or and Ghezzehei (2000) modeled evaporation from individual water droplets attached to cavity ceilings, assuming constant temperature and humidity conditions. In the present study, we extend these evaporation models to account for evaporation from a variably saturated porous surface. In contrast to the positive capillary pressure on the surfaces of evaporating droplets, the porous surface typically has negative or zero capillary pressure. The evaporation model used in this study is coupled with flow in the porous medium, and the RH of the ambient air could vary.

The formulation we used capitalizes on the observed dependence of evaporation rate on cavity humidity and ventilation conditions, and the availability of high resolution time-series data of RH, temperature, and free-water evaporation rate (Trautz and Wang, 2002).

In the following subsections, we introduce an isothermal vapor diffusion model of evaporation and define the problem domain and boundary conditions. This is followed by estimation of the evaporation model parameters using free-water evaporation data. Finally, a remark on evaporation from a porous surface is provided.

Isothermal Vapor Diffusion Model

The development of the isothermal vapor diffusion model presented in this section closely follows that of Ho (1997), with the exception of the range of vapor pressure on the evaporating surface. In the study of Ho (1997) the vapor pressure on the surface of the evaporating pendent drops depends on the drop radius (positive capillary pressure), while in our study the vapor pressure on the surface of the porous medium depends on the capillary pressure of the liquid held in the pores (negative or zero capillary pressure). To simplify the first step of evaporation (vaporization) we assume the following:

- The absorption of latent heat and its effect on the physical properties of the liquid–vapor interface are negligible.
- The time dependence of the vaporization process (e.g., Zhang and Wang, 2002; Zhang et al., 2001) is neglected.
- The vapor partial pressure of the interfacial air is assumed to be under thermodynamic equilibrium.

At equilibrium, the air above a flat surface of pure water is considered saturated with vapor; its vapor pressure is denoted by p_s (Pa). This saturation vapor pressure rises with temperature. In the temperature range of -10 to

50°C , the saturation vapor pressure is related to interfacial temperature by (Murray, 1966)

$$\ln p_s = a \frac{T}{T + b} + c \quad [1]$$

where $a = 21.87$, $b = 265.5^\circ\text{C}$ and $c = 6.41$ are constants, and T ($^\circ\text{C}$) is the interfacial temperature. For nonflat interfaces (such as capillary menisci) the actual interfacial vapor pressure p is related to the interfacial capillary potential by the classic Kelvin equation:

$$\ln\left(\frac{p}{p_s}\right) = P_C \frac{M_w}{\rho_w R T} \quad [2]$$

where P_C (Pa) is the capillary pressure, $\rho_w = 998 \text{ kg m}^{-3}$ and $M_w = 0.018 \text{ kg mol}^{-1}$ are the density and molecular mass of liquid water, respectively; and $R = 8.3143 \text{ J K}^{-1} \text{ mol}^{-1}$ is the universal gas constant. Note that the RH of air is defined as the ratio of the actual partial pressure p to the saturated vapor pressure p_s :

$$h = p/p_s \quad [3]$$

The second step of evaporation, vapor removal from the interface, is modeled as a first-order phenomena described by Fickian diffusion (Rohsenow and Choi, 1961). In one dimension and under constant temperature, the vapor mass flux J_v ($\text{kg m}^{-2} \text{ s}^{-1}$) is given by

$$J_v|_T = -D_v \frac{dC}{dz} \quad [4]$$

where D_v ($\text{m}^2 \text{ s}^{-1}$) is the vapor diffusion coefficient, which is related to the ambient air pressure, P (Pa), and air temperature T by (Vargaftik, 1975)

$$D_v = 2.13 \times 10^{-5} \frac{10^5}{P} \left(\frac{T}{273.15}\right)^{1.8} \quad [5]$$

and the vapor concentration C (kg m^{-3}) is related to vapor pressure by

$$C = \frac{M_w}{RT} p \quad [6]$$

Note that the error introduced by the equimolar counterdiffusion equation (Eq. [4]) to represent evaporation (vapor diffusion in stationary gas) is ignored. In the subsequent subsection, we define the problem domain and develop the appropriate boundary conditions needed to solve the vapor diffusion Eq. [4].

Velocity and Concentration Boundary Layers

In admitting diffusive flux as the primary mechanism for vapor removal from the evaporating surface, we assume that airflow above the evaporating surface is fully developed and laminar, as illustrated in Fig. 1a. The free-stream air velocity, U^∞ (m s^{-1}), is retarded in the vicinity of the evaporating surface because of frictional resistance. The air velocity parallel to the evaporating surface increases from $U = 0$ at $z = 0$ (no-slip) asymptotically to $U = U^\infty$ at a distance sufficiently far away from the surface. For fully laminar flow conditions, the thickness of the boundary layer (δ_U) of re-

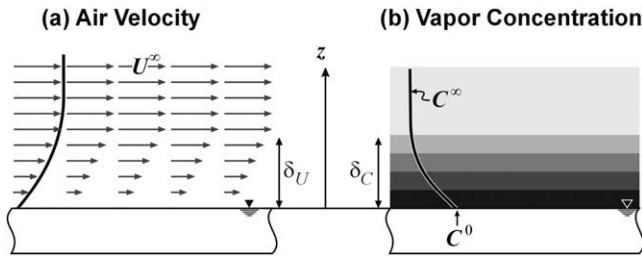


Fig. 1. Schematic description of (a) air velocity and (b) vapor concentration profiles above a free water surface.

tarded velocity (defined as $U \leq 0.99U^\infty$) is inversely proportional to the square root of the free-stream velocity (Rohsenow and Choi, 1961):

$$\delta_U \propto 1/\sqrt{U^\infty} \quad [7]$$

Because the equations that describe laminar air flow parallel to a flat surface and diffusion from a flat surface are analogous (Rohsenow and Choi, 1961), a similar notion of concentration boundary layer holds near the evaporating surface. The vapor concentration profile is illustrated in Fig. 1b. The vapor concentration decreases from an equilibrium value ($C = C^0$) at $z = 0$ to a value determined by the free-stream humidity at sufficiently far distance. The concentration boundary layer thickness (δ_C) is related to the velocity boundary layer thickness by the Schmidt number:

$$S_c = \frac{\delta_C}{\delta_U} = \frac{\mu_a}{\rho_a D_v} \quad [8]$$

where μ_a (Pa s) and ρ_a are the viscosity and density of air, respectively. At 20°C and 1 atm pressure, the Schmidt number is approximately unity. In the remainder of this paper the subscripts in the boundary layer thickness are dropped and $\delta = \delta_U = \delta_C$ (m). It is evident from Eq. [7] and [8] that the concentration BLT (δ) is inversely related to the square root of the free-stream velocity (U^∞) and can serve as a direct measure of the cavity ventilation condition. In a subsequent subsection, estimation of the BLT will provide further elaboration on the dependence of δ on ventilation conditions.

Boundary Conditions

The domain of the vapor diffusion Eq. [4] is the concentration boundary layer introduced in the preceding section. The boundary condition on Eq. [4] corresponding to the equilibrium vapor concentration at the evaporating surface ($z = 0$) is given by (using Eq. [2] and [6]):

$$C = C^0 = \frac{M_w}{RT} p_s \exp\left(\frac{P_c M_w}{\rho_w RT}\right) \quad [9]$$

The second boundary condition is at the border of the concentration boundary layer $z = \delta$, where the vapor concentration is defined by the RH (h) of the ambient air:

$$C = C^\infty = \frac{M_w}{RT} p_s h \quad [10]$$

If the boundary conditions change slowly, the evapora-

tion rate can be considered to be at steady state and the concentration gradient dC/dz is constant throughout the boundary layer. Then, the steady-state vapor diffusion Eq. [4] under isothermal conditions is simplified to

$$J_v = D_v \frac{C^0 - C^\infty}{\delta} \quad [11]$$

Note that the ratio δ/D_v is commonly referred to as diffusional resistance, and Eq. [11] is essentially Dalton's equation as used by Penman (1948). The isothermal vapor diffusion Eq. [11] is considered valid for modeling evaporation from cavity surfaces and free water. Fujimaki and Inoue (2003) found Eq. [11] (also known as the bulk transfer equation) to be valid in laboratory evaporation experiments in which the ambient air velocity was on the order of 1 m s⁻¹. All the variables of this model are directly related to physical conditions in the cavity, and all of them, except δ , can be independently determined from measured quantities. The boundary layer thickness (δ) can be estimated by calibrating Eq. [11] against free water evaporation data, as discussed in the next section.

Estimation of the Boundary Layer Thickness

Apart from the capillary pressure at the evaporating surface, evaporation from free water and that from a wet porous surface are thus far assumed to be identical processes. Therefore, a controlled evaporation experiment from a still-water surface can be used to estimate the vapor concentration boundary layer thickness, which is also applicable to evaporation from wet cavity surfaces at similar ventilation conditions. Upon substitution of Eq. [1], [5], [9], and [10] in Eq. [11], and noting that the capillary pressure of the free-water surface is $P_c = 0$, we arrive at a free-water evaporation equation:

$$J_v = 2.13 \times 10^{-5} \frac{10^5}{P} \left(\frac{T}{273.15}\right)^{1.8} \exp\left(a \frac{T}{T+b} + c\right) \frac{M_w}{RT} \frac{1-h}{\delta} \quad [12]$$

According to the isothermal assumption, T denotes the temperature of the evaporating surface and the surrounding air. Assuming the change in conditions that affect evaporation rate is slow compared with the time it takes to reach steady-state evaporation, Eq. [12] can be fitted to time-series data of evaporation rate data measured at known temperature, pressure, and RH conditions. The best-fit δ represents the boundary layer thickness at the prevailing ventilation condition. However, it should also be noted that uncertainties associated with the assumed simplifications (including isothermal conditions, flat evaporating surface, and laminar airflow) are lumped into this parameter. Thus, the boundary layer thickness should be considered an effective parameter.

Evaporation from Porous Surface

The surface of an unsaturated porous medium typically consists of solid (matrix of the medium) and pore

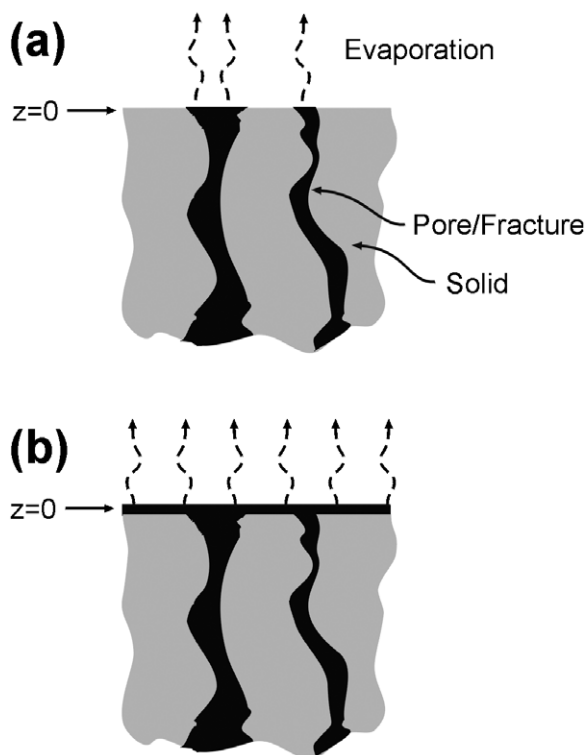


Fig. 2. Evaporating surface area of a porous medium: (a) partitioning of the surface into nonevaporating solid and evaporating pores; (b) proposed approach of uniform liquid-phase surface. The dark shading denotes vapor in pores and/or fractures.

and fracture (liquid and gas) components, rendering the evaporating surface heterogeneous with respect to vapor concentration, as illustrated in Fig. 2a. During seepage, however, cavity ceilings are usually covered with liquid films (e.g., Trautz and Wang, 2001), and the vapor concentration could be considered locally homogeneous. For simplicity, we extend this assumption of locally uniform distribution of vapor concentration to the entire cavity Fig. 2b. The vapor concentration at any given location on the cavity is assumed to be at capillary equilibrium with the pores and fractures of the porous medium. The datum $z = 0$ for the vapor diffusion is set on the surface of the cavity (as illustrated in Fig. 2b). Although this assumption is likely to fail at very low saturations (when the liquid is scattered in a few fine pores and fractures), it is expected to be of marginal consequence because the evaporation rate under such conditions is very low. Moreover, as indicated in the preceding section, uncertainties regarding the geometry of the evaporating pan are lumped into the calibrated boundary layer thickness. It should be noted that an unknown error is introduced when applying this boundary layer thickness value to evaporation from rough cavity surfaces that have significantly different geometry from the relatively flat free water surfaces.

COUPLED SEEPAGE AND EVAPORATION

In a cavity constructed in unsaturated formations, the flow velocity of water in the rock is usually stagnated

near the crown, resulting in an elevated moisture content in this region (Philip et al., 1989b). Unlike evaporation from a ground surface, where infiltration opposes the evaporation flux, the condition in cavities is favorable for simultaneous occurrence of evaporation and seepage. Field tests that exhibit simultaneous evaporation and seepage are described below. After field-test descriptions, we present a brief description of seepage modeling using the numerical simulators TOUGH2 (Pruess et al., 1999) and iTOUGH2 (Finsterle, 1999) and discuss implementation of evaporation in these models.

MATERIALS AND METHODS

Field Tests

The data reported in this paper were obtained from field tests and measurements conducted at the proposed nuclear waste repository at YM currently under investigation by the USDOE. Air-injection tests were conducted to characterize the permeability and small-scale heterogeneities of the formation, and liquid-release tests were performed to study seepage phenomena. RH, temperature, and free-water evaporation were monitored at the test site to assess the evaporation conditions. Detailed description of the site and tests conducted at the site are provided elsewhere (Birkholzer et al., 1999; Bodvarsson et al., 1999; Finsterle and Trautz, 2001; Finsterle et al., 2003; Trautz and Wang, 2001, 2002; Wang et al., 1999). This study is concerned with the lower lithophysal welded tuff unit at YM, in which about 80% of the proposed repository is expected to reside. This unit contains many small fractures (<1 m long) and is interspersed with numerous lithophysal cavities (0.15–1 m diam.).

In the lower lithophysal unit, an 800-m-long drift (5-m diam.) for enhanced characterization of the repository block (ECRB) was excavated. Liquid-release and air-injection tests were systematically conducted in this ECRB Cross Drift along boreholes drilled into the ceiling of the Cross Drift at regular intervals. Similar tests were conducted in a short (≈ 15 m long) drift excavated off the Cross Drift (niche). Schematic alignment of the cavities is shown in Fig. 3a. This paper is concerned with tests conducted at a Cross Drift borehole designated as LA#2 (Fig. 3b) and a short drift known as Niche 5 (Fig. 3c). The tests and measurements conducted in the Cross Drift and Niche 5 are briefly described below. In the remainder of this paper, drifts and niches are referred to by the generic term *cavity*.

Air-Injection Tests

The purpose of the air-injection tests was to estimate absolute permeability of the formation as a basis for the stochastic generation of heterogeneous permeability fields. Short sections of the boreholes (0.3 m in Niche 5, 1.8 m in the Cross Drift) were isolated using an inflatable packer system, and compressed air was injected. Air injection was terminated when steady-state pressure was reached. Air-permeability values were derived from the steady-state pressure data according to an analytical solution of LeCain (1995). Permeabilities determined from air-injection tests were considered representative of the absolute permeability of the test interval because the air-injection tests were conducted in a network of essentially dry fractures before the liquid-release tests were conducted. Therefore, no empirical relative permeability function is needed to translate air conductivity into absolute permeability.

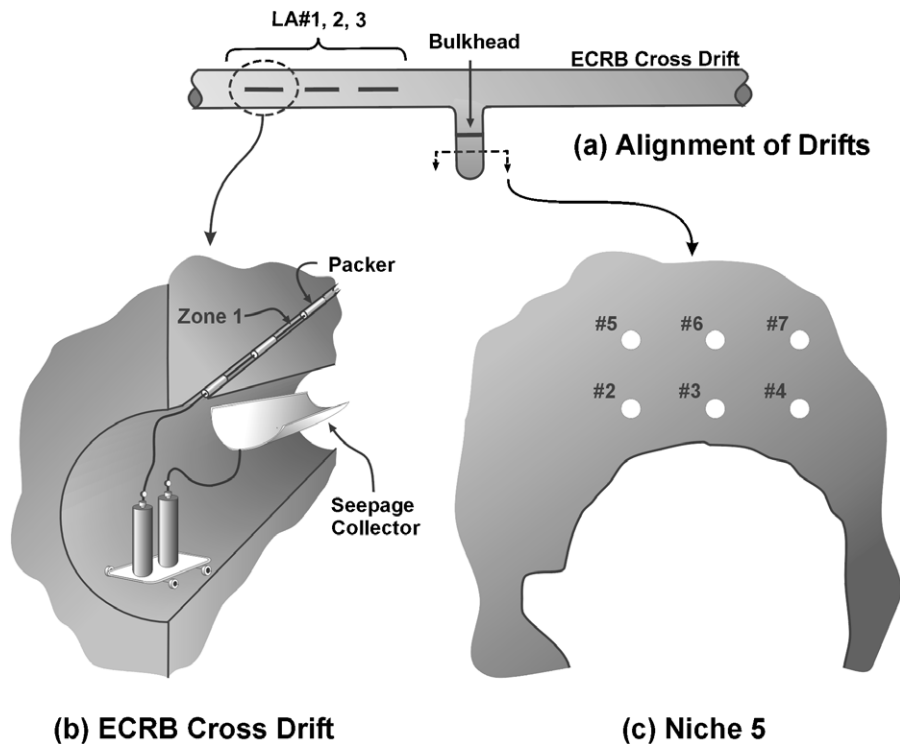


Fig. 3. Schematic alignment of cavities and boreholes: (a) part of the enhanced characterization of the repository block (ECRB) Cross Drift; (b) liquid release test setup in the Cross Drift, including liquid release intervals and liquid injection and seepage collection equipment; and (c) vertical section of Niche 5 along with location of all the test boreholes.

Liquid-Release Tests

Liquid-release tests were conducted in boreholes drilled above cavities to evaluate seepage into waste emplacement drifts. The alignment of the boreholes and test intervals are schematically shown in Fig. 3. The liquid-release boreholes in the Cross Drift were approximately 20 m long, drilled into the ceiling of the Cross Drift at a nominal inclination of 15° from the horizontal. Liquid-release data from Borehole LA#2 were used in this study. The borehole was partitioned into three zones (designated as Zones 1, 2, and 3) available for liquid release testing. The distances from the middle of the liquid-release zones to the drift crown were 1.58, 2.84, and 4.10 m for Zones 1, 2, and 3, respectively. The liquid-release boreholes in Niche 5 were near horizontal. In this study, we used data from tests (Boreholes 4 and 5) that lasted long enough to achieve nearly steady-state seepage. The liquid-release tests were performed by injecting water into a test interval isolated by inflated rubber packers. Water that seeped into the cavities was captured and measured using automated recording devices.

Relative Humidity and Temperature Measurements

The Cross Drift was actively ventilated during regular working hours, thus the RH of the cavity was usually low. Because the primary objective of the liquid-release tests was to calibrate the seepage models, minimization of evaporation was an essential component of the tests. To mitigate the effect of evaporation in the seepage process, the seepage collection interval of the Cross Drift was guarded using curtains on both ends. The RH in Niche 5 was relatively high because it was isolated from the actively ventilated Cross Drift by a bulkhead. To aid in the estimation of evaporation during the liquid-release tests, the RH and temperature of the air inside and outside of the curtains (for the Cross Drift) and in front of and behind the

bulkhead (for Niche 5) were monitored using Vaisala HMP45C probes (Vaisala Inc., Helsinki, Finland) (RH measurement range 0–100% noncondensing, accuracy at 20°C ± 2% for 0–90% RH and ±3% for 90–100% RH; temperature measurement range –40 to 60°C, accuracy ±1%). Up to 11 sensors were distributed in different parts of the cavities, and averaged values are reported here.

The evaporation rate from still water was measured by monitoring the level (mass) of water in evaporation pans placed within the space enclosed by the seepage capture tray and end curtains (for the Cross Drift tests) and behind the bulkhead (for Niche 5).

TOUGH2/iTOUGH2 SEEPAGE MODEL

A detailed description of the numerical models developed for flow in a fractured formation around a cavity and associated seepage into the cavity using TOUGH2/iTOUGH is given by Finsterle et al. (2003). A summary of the seepage model follows.

We are concerned with the effective seepage behavior on the scale of a drift segment rather than with individual seepage events from specific dripping locations. Thus, the unsaturated flow through the densely fractured formation and seepage into the cavities is represented by a simplified, heterogeneous continuum model. The matrix is not explicitly represented in this single-continuum model because its contributions to flow and seepage are expected to be small. The effects the matrix and microfractures are accounted for through the estimation of effective parameters (Finsterle et al., 2003).

The TOUGH2 module we used (EOS9) is an integral finite difference simulator that represents unsaturated

flow at the scale of individual gridblocks by Richards' equation (Bear, 1972; Pruess et al., 1999)

$$\phi\rho\frac{\partial}{\partial t}S_e = \text{div}\left[k\frac{\rho}{\mu}\nabla(P_C + \rho gz)\right] \quad [13]$$

where ρ and μ are the density and viscosity of water, ϕ is the porosity, and the effective saturation, S_e , is defined as $S_e = (S - S_{ir})/(1 - S_{ir})$, with S_{ir} being the residual liquid saturation. The appropriateness of using this continuum approach to simulate water flow through unsaturated fractured rock was shown by Finsterle (2000). The effective permeability, k (m^2), and capillary pressure, P_C , are functions of liquid saturation as given by van Genuchten's models (1980)

$$k = k_a S_e^{1/2} [1 - (1 - S_e^{1/m})^m]^2 \quad [14]$$

$$P_C = -\frac{1}{\alpha} [S_e^{-1/m} - 1]^{1-m} \quad [15]$$

where k_a is the absolute permeability, and $1/\alpha$ (Pa) and m are fitting parameters with $\alpha > 0$ and $0 < m < 1$. While the k_a were considered spatially heterogeneous, the $1/\alpha$, m , and S_{ir} parameters were assumed to be homogeneous for a given test bed (Finsterle et al., 2003). The absolute permeability, k_a , was derived from the air-injection tests. The van Genuchten m parameter and the residual saturation were taken to be $m = 0.608$ and $S_{ir} = 0.01$, respectively (Finsterle et al., 2003). The van Genuchten capillary strength parameter $1/\alpha$ was estimated through inverse modeling. In the numerical seepage model, the condition for seepage is determined by the total water-potential gradient at the connection between the porous medium and the cavity, as depicted in Fig. 4. The mass flux of seepage water J_w ($\text{kg m}^{-2} \text{s}^{-1}$) along the connection between the porous medium and the cavity is given by

$$J_w = -k \frac{\rho}{\mu} \frac{\Delta P + \rho g \Delta z}{\Delta z} \quad [16]$$

where ΔP denotes the capillary pressure difference across the distance between the last formation node and the cavity node $\Delta z = 0.05$ m. From Eq. [16], and assuming that the capillary pressure in the opening is zero, it follows that downward seepage ($J_w > 0$) occurs only when the following condition is satisfied:

$$-P_c^* > \rho g \Delta z \quad [17]$$

where P_c^* is the threshold capillary pressure at the last node adjacent to the opening. The critical capillary pressure $P_c^* > -\rho g \Delta z$ depends on the grid size or nodal distance of the numerical model. Thus, the applicability of the calibrated $1/\alpha$ parameter is limited to the specific numerical scheme used during calibration (Finsterle et al., 2003). According to Eq. [17], the cavity surface does not need to be fully saturated for seepage to commence as in the case of unfractured homogeneous porous media (Philip et al., 1989b).

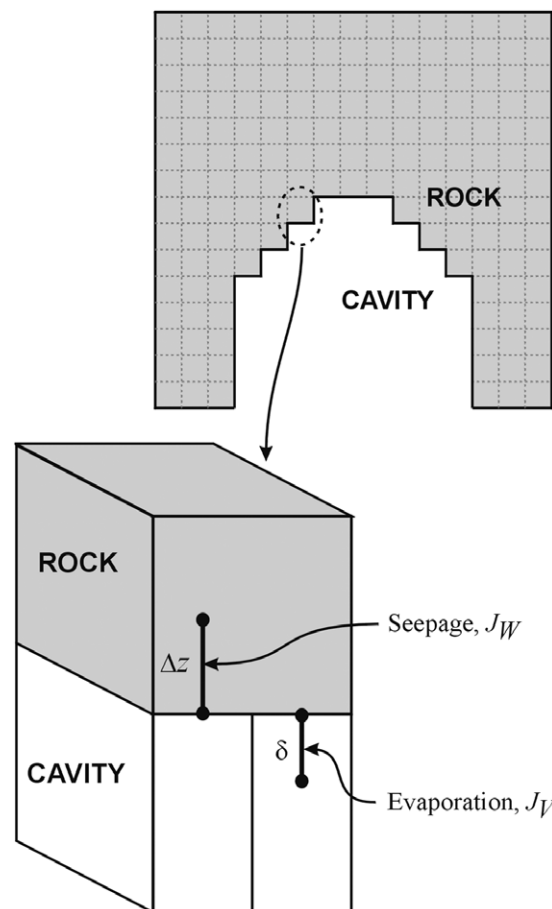


Fig. 4. Schematic description of the overlapping seepage and evaporation gridblocks and the respective connections with the gridblock that represents the cavity wall.

Implementation of Evaporation in TOUGH2

While seepage occurs only when the critical condition given in Eq. [17] is satisfied, vapor flow from/to cavity walls to/from cavity air occurs as long as there is vapor pressure disequilibrium between them. Coupling of the seepage and evaporation processes is illustrated in Fig. 4. Mass-transfer rate of water, including seepage, is represented in TOUGH2 by equations similar to Eq. [16], where the driving force is pressure gradient. To incorporate evaporation into the existing iTOUGH2 model without significant changes to the governing flow equations, the concentration gradient-dependent diffusion Eq. [11] was rewritten in the form of Eq. [16]. Thus, for the purpose of evaporation from the cavity walls, the nodal distance Δz is equivalent with the vapor concentration boundary layer thickness δ . Then, equating Eq. [11] and [16] and rearranging gives

$$k_{eq} = D_v \frac{\mu}{\rho} \frac{(C^0 - C^\infty)}{(P_c^0 - P_c^\infty)} \quad [18]$$

where the variables with a superscript zero correspond to the cavity wall and those with a superscript ∞ denote the cavity air. The capillary pressure of the cavity P_c^∞ is equivalent to the RH of the cavity (Eq. [3]), as described by Kelvin's Eq. [2]. The vapor concentrations are computed according to Eq. [9] and [10]. Equation [18] was

implemented in iTOUGH2 as an equivalent permeability for the special evaporation connections. Note that k_{eq} is merely a numerical trick used to represent the concentration gradient-based vapor diffusion equation using the capillary pressure gradient-based flow equations used in iTOUGH2. When the conditions for both evaporation and seepage permit, the total mass flow from the cavity wall to the cavity is considered as the sum of both.

Numerical Meshes

Different numerical models were constructed to simulate liquid-release tests and seepage into the under-

ground openings at different test locations. Three-dimensional meshes of the test sites were generated with grid sizes of 0.3 by 0.1 by 0.1 m for the Cross Drift and 0.1 by 0.1 by 0.1 m for Niche 5 (Fig. 5). The total mesh size of the models was on the order of 100 000 gridblocks. For the Cross Drift meshes, a 5-m diameter, cylindrical cavity was removed from the center of the mesh to represent the cavity. Only one-half of the symmetric mesh was used in the simulations to save computational load. For the Niche 5 meshes, surveyed niche geometry was removed from the numerical mesh to replicate the test sites. The liquid-release boreholes are indicated in Fig. 5 by bold black lines, and the white sections at the

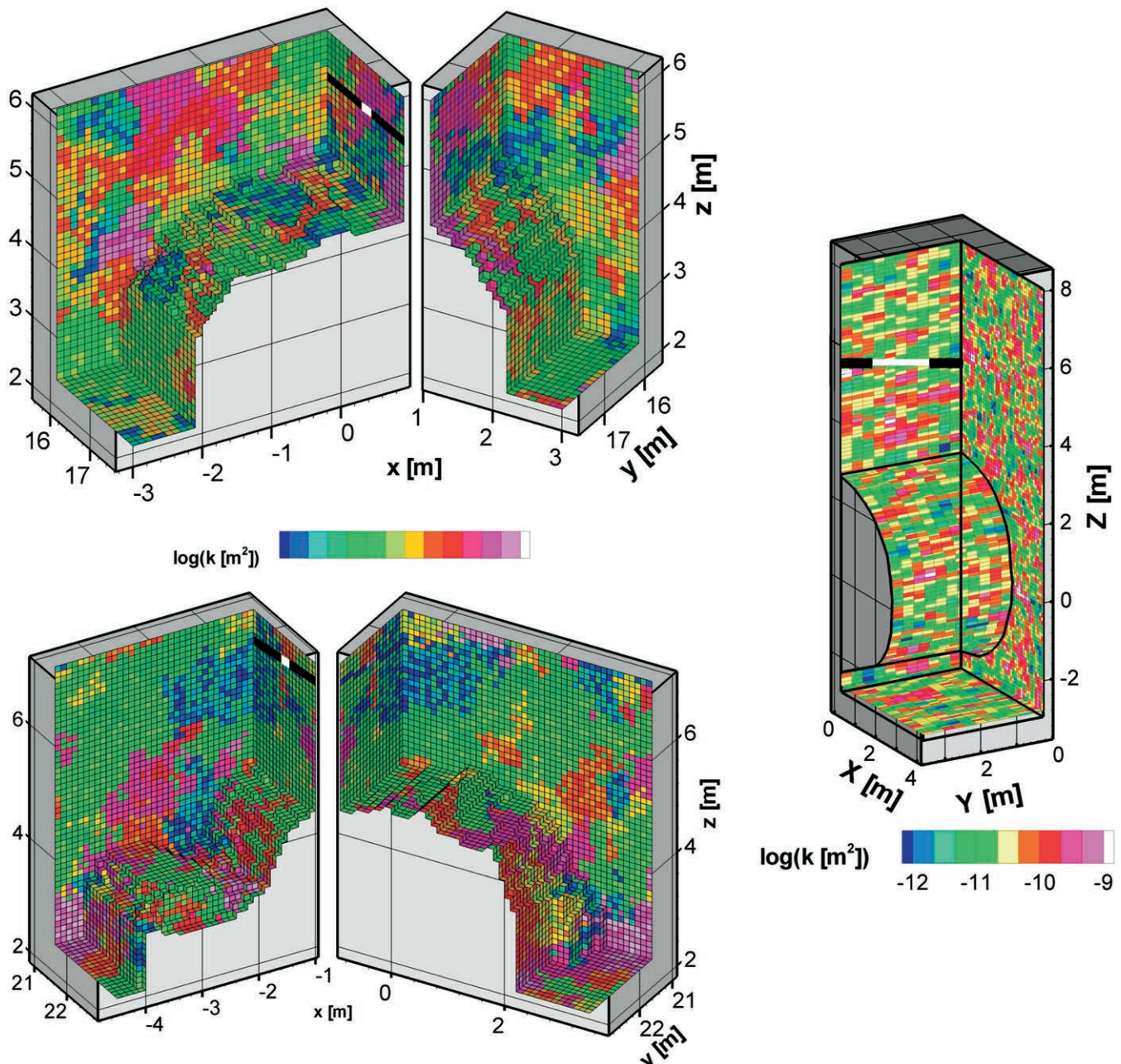


Fig. 5. Numerical meshes of (a) Niche 5 with Borehole 4, (b) Niche 5 with Borehole 5, and (c) the Cross Drift, along with a typical realization of the correlated stochastic permeability field. Bold black lines denote the liquid-release boreholes; the white section in the middle of the boreholes is the injection interval.

Table 1. Mean, standard deviation, and correlation length of log-permeability data collected in the Cross Drift and Niche 5. The spherical variogram parameter values for the Cross Drift were prescribed because the number of measurements was not adequate to compute the parameters.

Location	<i>n</i>	Mean log(<i>k</i>)	SD	Spherical variogram		
				Sill value	Correlation length	Nugget effect
		— m ² —	log(<i>k</i>) ²	m	log(<i>k</i>) ²	
Niche 5	61	-10.95	1.31	1.81	0.91	0.02
Cross Drift	6	-10.73	0.21	1.0	0.2	-

middle of the boreholes represent the injection intervals. The Cross Drift borehole is inclined, while the Niche 5 boreholes are parallel to the centerline of the niche. The Cross Drift mesh in Fig. 5a represents the Zone 2 test interval. Figures 5b and 5c illustrate Boreholes 4 and 5, respectively (see also Fig. 3c). Notice that the injection intervals in Boreholes 4 and 5 are located at 3 to 3.5 and 8.5 to 8.8 m, respectively, from the borehole collars; hence, the respective niche outlines are different.

The spatial structure of the Niche 5 permeability data was analyzed using the GSLIB module GAMV3 (Deutsch and Journel, 1992) and a spherical semivariogram was fitted to the resulting variogram.

In the Cross Drift six air-injection tests were performed in borehole intervals approximately 1.8 m in length, providing an estimate of mean log-permeability at the experimental site of -10.73 (corresponding to a permeability of 1.86×10^{-11} m²) with a standard deviation of 0.21. Variability in permeability on the scale of a gridblock (which is 0.3 m long) is expected to be higher than the measured standard deviation. For the purpose of generating a heterogeneous field, permeability is taken to be lognormally distributed with a standard deviation of one order of magnitude. Because the number of data points was insufficient to reveal the spatial correlation structure of the permeability field, a weak spatial correlation of 0.2 m was prescribed, consistent with the geostatistical results reported by Finsterle et al. (2003). The computed and prescribed geostatistical

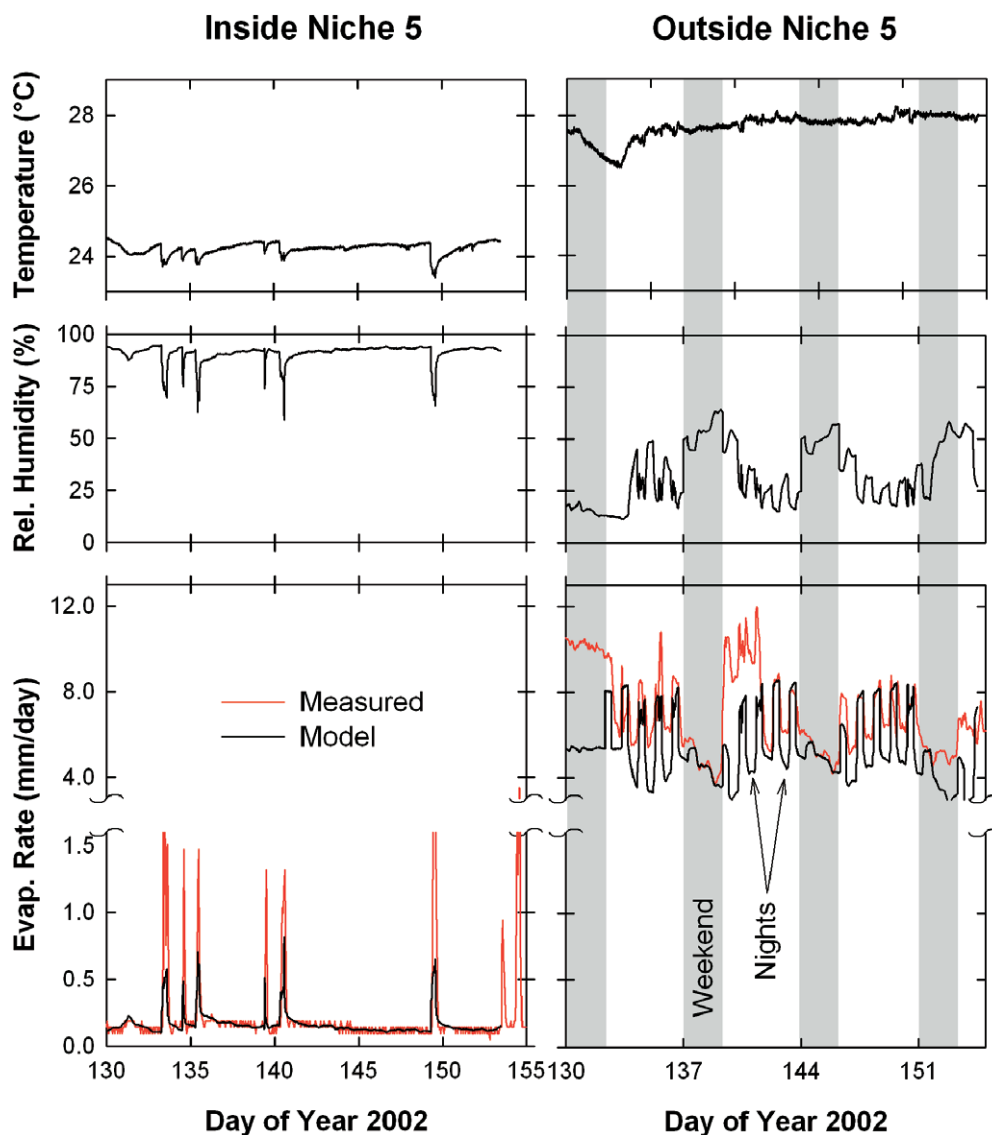


Fig. 6. Temperature, humidity, and evaporation rate data, along with model fit of the evaporation data for inside and outside of Niche 5.

Table 2. Summary of estimated boundary layer thicknesses for Niche 5 and their application.

Location of experiment	δ	Used for simulation of liquid-release tests in
	mm	
Inside Niche 5	20.0	Niche 5
Outside Niche 5, ventilation off	7.5	Cross Drift (with end curtains)
Outside Niche 5, ventilation on	5.0	Not used

parameters are reported in Table 1. These parameters were used to constrain generation of spatially correlated permeability fields, using the Gaussian sequential indicator simulation (SISIM) module of the GSLIB (Deutsch

and Journel, 1992). Multiple realizations of the permeability field were generated and mapped to the numerical meshes. Representative permeability field realizations for the Cross Drift and Niche 5 are shown in Fig. 5.

The cavities were represented in the seepage models by two types of overlapping gridblocks, one corresponding to seepage and the other to evaporation as shown in Fig. 4. The seepage gridblocks were assigned a zero capillary pressure, whereas the evaporation gridblocks were assigned a capillary pressure and vapor concentration corresponding to the cavity RH, as given by Eq. [2] and [3]. No-flow boundary conditions are specified at the left, right, front, and back sides of the model. A free-drainage boundary condition is applied at the bottom to prevent an unphysical capillary boundary effect.

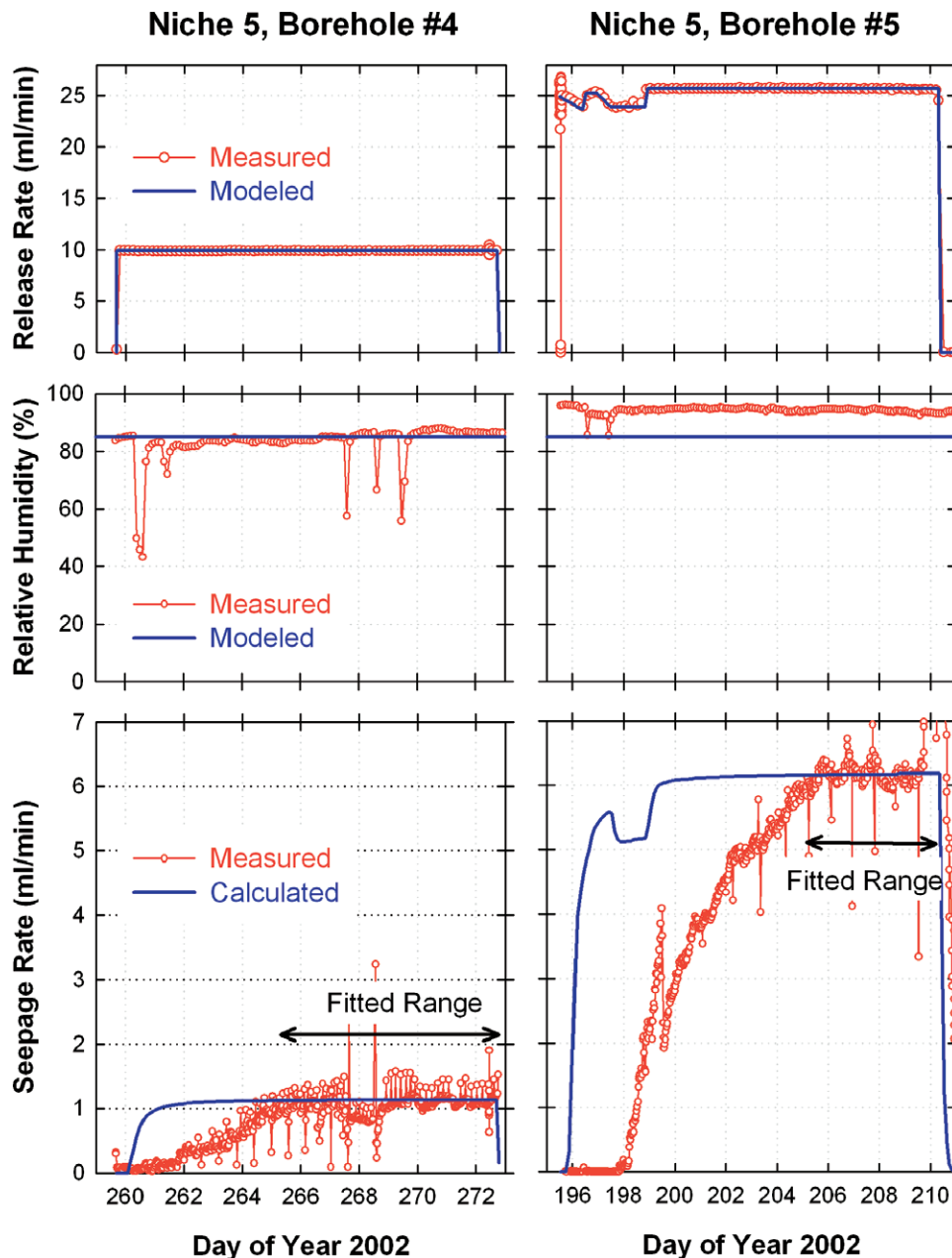


Fig. 7. Calibration of seepage-rate data from liquid-release tests conducted in Niche 5. Calculated seepage rate curves show only one of the multiple inversions.

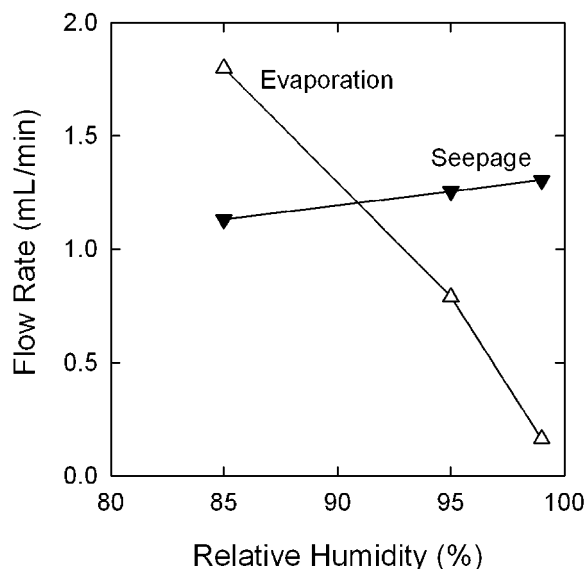


Fig. 8. Effect of high relative humidity on evaporation and seepage rates.

RESULTS AND DISCUSSIONS

Evaporation Boundary Layer

The evaporation data collected in Niche 5 were used to calibrate the evaporation model. The data were grouped into three classes based on airflow velocity (ventilation): (i) inside Niche 5 without ventilation, (ii) outside Niche 5 with active ventilation, and (iii) outside Niche 5 without active ventilation, the regime usually encountered during nights and weekends. In Fig. 6, the measured RH, and temperature, and evaporation rates from still water are plotted. The evaporation model (Eq. [12]) was fitted to the measured data by adjusting the boundary layer thickness. The RH and temperature measurements were conducted at a different time interval from the evaporation rate measurements. Thus, fitting was performed by matching the calculated and measured evaporation rates averaged over selected short durations of significance (such as continuous high or low evaporation rates). The estimates of the boundary layer thickness rounded to the nearest millimeter are listed in Table 2.

In agreement with the theoretical assessment (Eq. [7]), the estimated δ showed an inverse relationship with the ventilation conditions. Inside Niche 5, the air was the calmest because it was isolated from the Cross Drift by a bulkhead (see Fig. 3). As a result, the thickest boundary layer (20 mm) was obtained inside Niche 5. Figure 6 shows that the RH outside Niche 5 increases at nights and during weekends when active cavity ventilation is turned off. However, this increase in RH is insufficient to explain the observed decrease in evaporation. Therefore, as shown in Table 2, reduced air ventilation during nights and weekends is also accompanied by an increase in the thickness of the boundary layer. The estimated boundary layer thickness values and Eq. [7] suggest that the air velocity outside Niche 5 is higher than the inside by factors of 7 (without active ventilation) and 16 (with active ventilation).

Coupled Seepage and Evaporation

In this section, simulations of coupled seepage and evaporation are compared with measured seepage rate data. The software iTOUGH2 (Finsterle, 1999) was used to match the simulated seepage rate with the measured values by adjusting the free capillary strength parameter $1/\alpha$ (Finsterle et al., 2003). The corresponding evaporation rate from the cavity walls was simulated using the cavity RH and calibrated boundary layer thickness.

Niche 5

Two different data sets from liquid release tests conducted in Boreholes 4 (October 2002) and 5 (July 2002) are compared with the Niche 5 seepage models. The liquid release rate, seepage rate, and RH data as well as modeled liquid release rate and fitted seepage rate are shown in Fig. 7. The best-fit $1/\alpha$ values were 671 ± 223 and 740 ± 339 Pa for Boreholes 4 (30 inversions) and 5 (24 inversions), respectively. The measured seepage rates attained a steady-state flow rate after several days. Because the early-time transient data are biased by storage (e.g., in lithophysal cavities and matrix) and/or fast flow paths connecting the injection interval to the cavity ceilings, the model was fitted to the late-time steady-state data. In the simulations, the RH was kept constant at 0.85 to match with the lowest steady conditions observed during the Borehole 4 tests.

To quantify the impact of evaporation on seepage for the observed high RH range (0.85–0.99), the calibrated seepage model of Borehole 4 was used to simulate seepage and evaporation at RH values of 0.85, 0.95, and 0.99. The resulting steady-state seepage and evaporation rates (on Day 266) are plotted in Fig. 8. At a RH of 0.85, the evaporation rate from the entire niche wall surface and the seepage rate are comparable in magnitude. As the RH was increased, the steady-state evaporation rate showed a drastic decrease, while the corresponding seepage rate increased only slightly. Note that on Day 266 storage of liquid in the porous medium does not play a role on the water balance because steady-state flow is attained (see Fig. 7). Thus, these model results suggest that at high RH conditions the main impact of evaporation is on the quantity of liquid diverted around the cavity.

ECRB Cross Drift

We compare two different data sets from liquid release tests conducted in Borehole LA2, Zone 2, and Zone 3 with the ECRB Cross Drift seepage model. The liquid release rate, seepage rate, and RH data, as well as modeled liquid-release rates and fitted seepage rates, are plotted in Fig. 9. The best-fit capillary-strength parameters, $1/\alpha$, were 557 ± 56 Pa for Zone 2 and 535 ± 58 Pa for Zone 3, based on 21 and 19 inversions, respectively. Note that both of the liquid-release tests were conducted concurrently. The measured and simulated seepage-rate fluctuations were strongly correlated to the drastic changes in RH, and hence, evaporation. The

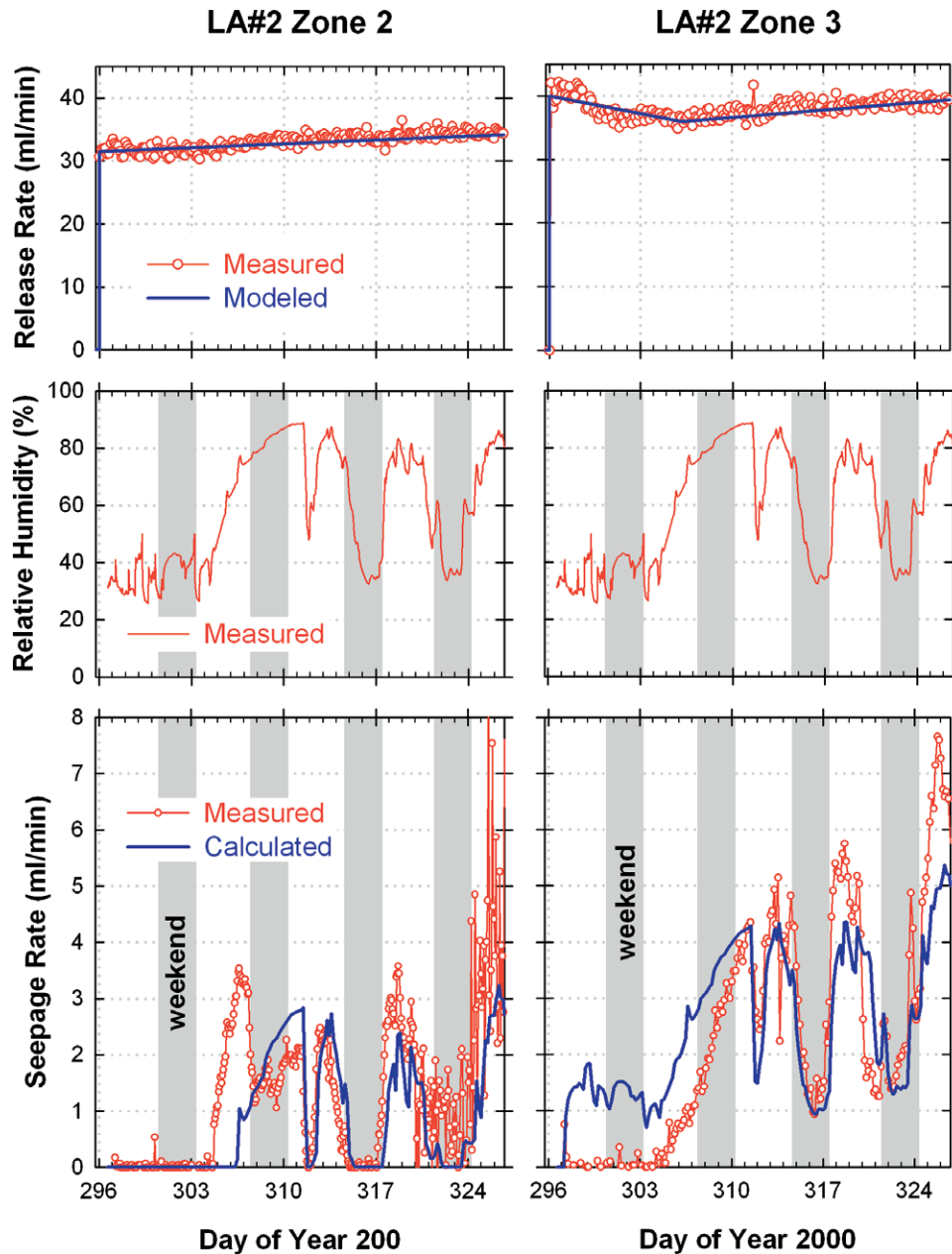


Fig. 9. Calibration of seepage-rate data from liquid-release tests conducted in the Enhanced Characterization of the Repository Block (ECRB) cross drift. Calculated seepage rate curves show only one of the multiple inversions.

model captured this evaporation effect satisfactorily, tracking increases in measured seepage rates as RH increased and vice versa.

The interplay between RH fluctuation and dynamics of flow and ceiling wetness at different times during the test in Zone 2 are illustrated in Fig. 10. During this test, the liquid release rate was relatively stable (steadily increasing from $\approx 31 \text{ mL min}^{-1}$ on Day 296 to $\approx 34 \text{ mL min}^{-1}$ on Day 327). However, the RH fluctuated between 30 and 90% during this time. Figure 10 shows snapshots of the liquid saturation distribution on Days 296, 306, 316, and 326. Just before the test began, the drift wall had dried out because of low RH in the drift. The liquid saturation at this time was in equilibrium with the assumed background percolation flux of 2 mm yr^{-1} . On Day 306 of injection (RH $\approx 70\%$), water reached

the crown of the drift, seepage had started, water was being diverted around the drift, and the wet plume had reached approximately midway around the drift. After 20 d (Day 316), however, the plume had shrunk significantly because of reduced humidity ($\approx 38\%$) and increased evaporation. Moreover, the seepage rate and seepage locations (indicated by inverted triangles) had decreased. On about Day 326, the RH rose up to approximately 80%. Thus, the evaporation rate was reduced, the wet plume grew, and seepage rate and number of seeps increased. In general, despite the high liquid release rate, the flow regime remained unsaturated. The liquid saturation was highest near the drift crown, which induces a capillary pressure gradient that promoted flow diversion around the drift (capillary barrier effect). Seepage and evaporation removed water from the for-

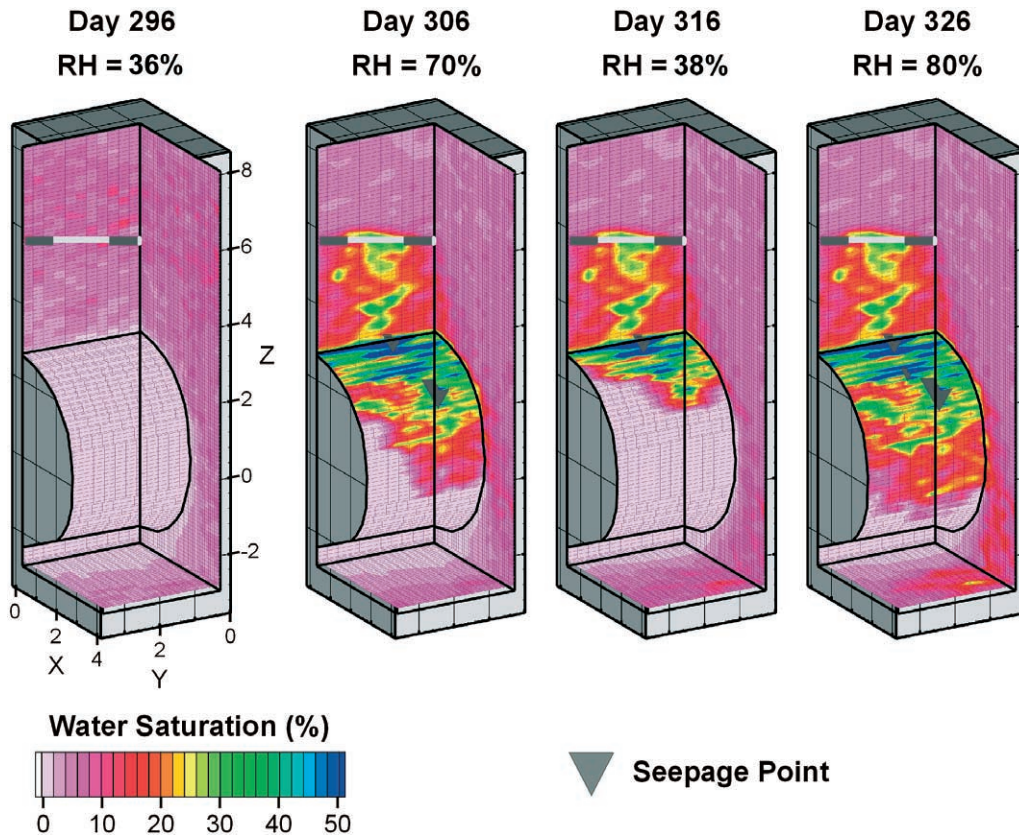


Fig. 10. Liquid saturation distribution simulated with model calibrated against seepage-rate data from liquid-release tests conducted in the Cross Drift Borehole LA#2, Zone 2 on Days 296, 306, 316, and 326. Note the correlation of cavity wall wetness to cavity relative humidity.

mation as water flowed around the drift, limiting the spread of the wetted region on the drift wall.

SUMMARY AND CONCLUSIONS

We (i) estimated the evaporative boundary layer thickness by calibrating a semiphysical evaporation model that considers isothermal vapor diffusion, (ii) calibrated a heterogeneous fracture-continuum model against seepage-rate data, and (iii) tested the effect of evaporation on seepage predictions. The major conclusions of this study are as follows:

1. The simplified vapor-diffusion approach of modeling evaporation was found to be effective in capturing the roles of the important environmental conditions that affect evaporation—namely, RH, temperature, and ventilation. Calibrated thicknesses of the evaporation boundary layer were obtained for three ventilation conditions representing the conditions at the liquid-release test sites at YM.
2. We found that evaporation reduces seepage significantly in tests conducted under ventilated conditions. Therefore, it is important to account for evaporation effects when calibrating a seepage process model against liquid-release test data collected under ventilated conditions. In contrast, the impact of evaporation on seepage rate was minimal in closed-off niches, where RH values were generally high. Thus, when using data obtained from closed-off and/or artificially humidified niches, ignoring the effect of evaporation is expected to introduce

little error in the estimation of seepage-relevant parameters.

3. The classification of ventilation regimes is based on crude assessment of the cavity environment. The effect of external wind velocity variations (note that the Cross Drift is connected to the air outside the ESF) was not accounted for in the calculations. The match between measured evaporation rate and model predictions could have been improved if accurate measurement of air velocity in the cavities had been made during the test.

The calibrated seepage models were tested by comparing blind predictions of seepage rates performed with the calibrated model against liquid release test data that were not used for model calibration. These model tests showed that the models predict seepage rate successfully according to a probabilistic acceptance criterion, which requires that at least 95% of the observed late-time seepage-rate data lie within the 95% simulation uncertainty band calculated by the calibrated model, or if the calibrated model overpredicts the seepage rates (deemed conservative). The model testing exercises and acceptance criterion are discussed in depth by Finsterle et al. (2003) and are not reported here.

ACKNOWLEDGMENTS

Thorough reviews and insightful comments by J. Birkholzer, G. Li, C.K. Ho, R. Fedors, C. Oldenburg, and an anonymous reviewer are gratefully acknowledged. This work was supported by the Director, Office of Civilian Radioactive Waste

Management, U.S. Department of Energy, through Memorandum Purchase Order QA-B004220RB3X between Bechtel SAIC Company, LLC, and the Ernest Orlando Lawrence Berkeley National Laboratory (Berkeley Lab). The support is provided to Berkeley Lab through the U.S. Department of Energy Contract no. DE-AC03-76SF00098.

REFERENCES

- Bear, J. 1972. Dynamics of fluids in porous media. Elsevier, New York.
- Birkholzer, J., G.M. Li, C.F. Tsang, and Y. Tsang. 1999. Modeling studies and analysis of seepage into drifts at Yucca Mountain. *J. Contam. Hydrol.* 38:349–384.
- Bodvarsson, G.S., W. Boyle, R. Patterson, and D. Williams. 1999. Overview of scientific investigations at Yucca Mountain—The potential repository for high-level nuclear waste. *J. Contam. Hydrol.* 38:3–24.
- Deutsch, C.V., and A.G. Journel. 1992. *GSLIB: Geostatistical software library and user's guide*. Oxford University Press, New York.
- Finsterle, S. 1999. *iTOUGH2 user's guide*. Rep. LBNL-40040. Lawrence Berkeley Natl. Lab., Berkeley, CA.
- Finsterle, S. 2000. Using the continuum approach to model unsaturated flow in fractured rock. *Water Resour. Res.* 36:2055–2066.
- Finsterle, S., C.F. Ahlers, R.C. Trautz, and P.J. Cook. 2003. Inverse and predictive modeling of seepage into underground openings. *J. Contam. Hydrol.* 62–63:89–109.
- Fujimaki, H., and M. Inoue. 2003. A transient evaporation method for determining soil hydraulic properties at low pressure. Available at www.vadosezonejournal.org. *Vadose Zone J.* 2:400–408.
- Finsterle, S., and R.C. Trautz. 2001. Numerical modeling of seepage into underground openings. *Min. Eng.* 53:52–56.
- Ho, C.K. 1997. Evaporation of pendant water droplets in fractures. *Water Resour. Res.* 33:2665–2671.
- Knight, J.H., J.R. Philip, and R.T. Waechter. 1989. The seepage exclusion problem for spherical cavities. *Water Resour. Res.* 25:29–37.
- LeCain, G.D. 1995. Pneumatic testing in 45-degree-inclined boreholes in ash-flow tuff near Superior, Arizona. USGS Water Resour. Invest. Rep. 95-4073. USGS, Denver, CO.
- Li, G.M., and C.-F. Tsang. 2003. Seepage into drifts with mechanical degradation. *J. Contam. Hydrol.* 62:157–172.
- Murray, F.W. 1966. On the computation of saturation vapor pressure. *J. Appl. Meteorol.* 6:204.
- Or, D., and T.A. Ghezzehei. 2000. Dripping into subterranean cavities from unsaturated fractures under evaporative conditions. *Water Resour. Res.* 36:381–393.
- Penman, H.L. 1948. Natural evaporation from open water, bare soil and grass. *Proc. R. Soc. London, Ser. A* 193:120–145.
- Philip, J.R. 1989a. Asymptotic solutions of the seepage exclusion problem for elliptic-cylindrical, spheroidal, and strip-shaped and disc-shaped cavities. *Water Resour. Res.* 25:1531–1540.
- Philip, J.R. 1989b. The seepage exclusion problem for sloping cylindrical cavities. *Water Resour. Res.* 25:1447–1448.
- Philip, J.R., J.H. Knight, and R.T. Waechter. 1989a. The seepage exclusion problem for parabolic and paraboloidal cavities. *Water Resour. Res.* 25:605–618.
- Philip, J.R., J.H. Knight, and R.T. Waechter. 1989b. Unsaturated seepage and subterranean holes—Conspectus, and exclusion problem for circular cylindrical cavities. *Water Resour. Res.* 25:16–28.
- Pruess, K., C. Oldenburg, and G. Moridis. 1999. *TOUGH2 user's guide*. Version 2.0. LBNL-43134. Lawrence Berkeley Natl. Lab., Berkeley, CA.
- Rohsenow, W.M., and H. Choi. 1961. *Heat, mass and momentum transfer*. Prentice Hall, Englewood Cliffs, NJ.
- Trautz, R.C., and J.S.Y. Wang. 2001. Evaluation of seepage into an underground opening using small-scale field experiments, Yucca Mountain, Nevada. *Min. Eng.* 53:41–44.
- Trautz, R.C., and J.S.Y. Wang. 2002. Seepage into an underground opening constructed in unsaturated fractured rock under evaporative conditions. *Water Resour. Res.* 38:(10)1188. doi:10.1029/2001WR000690.
- van Genuchten, M.Th. 1980. A closed-form equation for predicting the hydraulic conductivity of unsaturated soils. *Soil Sci. Soc. Am. J.* 44:892–898.
- Vargaftik, N.B. 1975. *Tables on the thermophysical properties of liquids and gases*. 2nd ed. John Wiley & Sons, New York.
- Wang, J.S.Y., R.C. Trautz, P.J. Cook, S. Finsterle, A.L. James, and J. Birkholzer. 1999. Field tests and model analyses of seepage into drift. *J. Contam. Hydrol.* 38:323–347.
- Zhang, J.T., and B.X. Wang. 2002. Effect of capillarity at liquid-vapor interface on phase change without surfactant. *Int. J. Heat Mass Transfer* 45:2689–2694.
- Zhang, J.T., B.X. Wang, and X.F. Peng. 2001. Thermodynamic aspect of the shift of concave liquid-vapor interfacial phase equilibrium temperature and its effect on bubble formation. *Int. J. Heat Mass Transfer* 44:1681–1686.